Standing Kink Waves in Sigmoid Solar Coronal Loops: Implications for Coronal Seismology

N. Magyar and V. M. Nakariakov
Centre for Fusion, Space and Astrophysics, Physics Department, University of Warwick, Coventry CV4 7AL, UK; norbert.magyar@warwick.ac.uk

Abstract

Using full three-dimensional magnetohydrodynamic numerical simulations, we study the effects of magnetic field sigmoidity or helicity on the properties of the fundamental kink oscillation of solar coronal loops. Our model consists of a single denser coronal loop, embedded in a plasma with dipolar force-free magnetic field with a constant α-parameter. For the loop with no sigmoidity, we find that the numerically determined oscillation period of the fundamental kink mode matches the theoretical period calculated using WKB theory. In contrast, with increasing sigmoidity of the loop, the actual period is increasingly smaller than the one estimated by WKB theory. Translated through coronal seismology, increasing sigmoidity results in magnetic field estimates that are increasingly shifting toward higher values, and even surpassing the average value for the highest α value considered. Nevertheless, the estimated range of the coronal magnetic field value lies within the minimal/maximal limits, proving the robustness coronal seismology. We propose that the discrepancy in the estimations of the absolute value of the force-free magnetic field could be exploited seismologically to determine the free energy of coronal loops, if averages of the internal magnetic field and density can be reliably estimated by other methods.

Unified Astronomy Thesaurus concepts: Magnetohydrodynamics (1964); Solar coronal seismology (1994); Magnetohydrodynamical simulations (1966)

1. Introduction

Coronal loops are the building blocks of the closed solar corona, appearing as bright arcs of plasma when viewed in extreme ultraviolet (e.g., Reale 2014). Understanding their formation and dynamics is essential in solving the long-standing coronal heating problem (e.g., Parnell & De Moortel 2012). Large-amplitude transverse (kink) oscillations of coronal loops were first reported by Aschwanden et al. (1999) and Nakariakov et al. (1999). These observations allowed for the previously theorized tool of coronal seismology (Uchida 1970; Roberts et al. 1984), applied first by Nakariakov & Ofman (2001), to emerge (see De Moortel 2005; De Moortel & Nakariakov 2012; Stepanov et al. 2012 for comprehensive reviews). In coronal seismology, observed wave properties, such as wave period, are compared to theoretical results, allowing plasma parameters that are hard to measure otherwise, such as magnetic field strength, to be inferred. Detailed knowledge of plasma properties is needed, e.g., for advancing the prediction of space weather events (e.g., Singh et al. 2010; Koskinen et al. 2017; Lanzerotti 2017).

For the first application of coronal seismology, the simplest theoretical model of a coronal loop was used (Zaitsev & Stepanov 1975; Edwin & Roberts 1983), comprising a straight flux tube with different constant Alfvén speeds inside and outside of the tube. In what followed, several additional effects that might change the oscillation properties were considered, such as varying Alfvén speed along the loop (Andries et al. 2005b; Arregui et al. 2005; Dymova & Ruderman 2005), variable cross section (Ruderman et al. 2008; Verth & Erdélyi 2008), elliptical cross section (Ruderman 2003), loop curvature (Van Doorsselaere et al. 2004; van Doorsselaere et al. 2009), loop shape (Selwa & Ofman 2010; Selwa et al. 2011a, 2011b), and twisted magnetic field (Ruderman 2007; Terradas & Goossens 2012; Ruderman & Terradas 2015), among others.

Oscillations in coronal loops that exhibited nonplanar geometry were first observed by Schrijver et al. (2002). Later it was determined that a significant portion of coronal loops are nonplanar, i.e., exhibiting a helical or sigmoid shape (Aschwanden et al. 2008, 2012; McKenzie & Canfield 2008; Syntelis et al. 2012; Zhou et al. 2016; Nisticò et al. 2017; Aschwanden 2019). The effect of nonplanar geometry of coronal loops on oscillation properties was first investigated by Ruderman & Scott (2011), who considered the loop axis to be a part of a helical line, and of the circular cross section. They found that the loop nonplanarity only weakly affects the estimates obtained through coronal seismology (Scott & Ruderman 2012), and that the simplest model of a straight homogeneous magnetic cylinder provides sufficiently accurate estimates. However, they used an asymptotic method with the ratio of the loop cross-section radius to the loop curvature radius as a small parameter. As stated by the authors, this implies that neither the loop curvature nor the loop twist can directly affect the period of the loop kink oscillations. Instead, the period was affected only indirectly through modifying the dependence of the density on the coordinate along the loop. Moreover, neither of these asymptotic results have been tested numerically nor has the interference of the effects of nonplanarity and the elliptic cross section been studied. Previous three-dimensional (3D) numerical simulations of coronal loop oscillations included the effects of curvature (Miyagoshi & Yokoyama 2004; Terradas et al. 2006; McLaughlin & Ofman 2008; Pascoe & De Moortel 2014), but maintained a planar loop geometry. In this study, we aim to improve on previous simulations of 3D curved coronal loop oscillations, by including the effect of nonplanarity, i.e., considering sigmoid coronal loops. This Letter is organized as follows: in Section 2, we present the numerical model and in Section 3, the method; in Section 4, the simulation results are
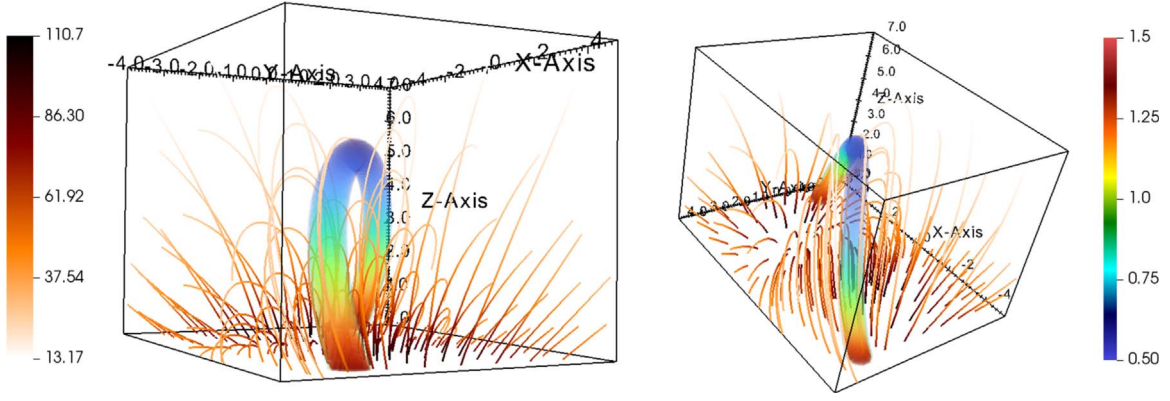
Figure 1. 3D views of the background magnetic field structure and the embedded higher-density loop, for $\alpha = 0.2$. The magnetic field is represented through streamlines of the vector field originating at the $z = 0$ plane. The color of the streamlines reflects the local magnetic field strength in Gauss. The loop is volume-rendered and the color represents density, in user units.

presented; and in Section 5, conclusions and implications for coronal seismology are drawn.

2. Numerical Model

The 3D numerical model consists of a background coronal plasma in a hydrostatic equilibrium in which we embed a coronal loop of higher density (see Figure 1). The magnetic field is produced by two magnetic constant-α "poles" of equal intensity and opposite signs located below the simulation region at $x_{0,1} = d$ and $x_{0,2} = -d$, respectively, along the $y = 0$, $z = -z_0$ axis. Here, α is the force-free parameter that controls the helicity of the field lines originating in the poles. The force-free magnetic field of a pole with constant α is given by (Chiu & Hilton 1977; Cuperman et al. 1989)

$$B_{x,j} = \frac{1}{r_j^2}\left[x_j \frac{r_j^2}{R_j^3}\cos(\alpha R_j) - \alpha \frac{x_j z_j^2}{R_j^2}\sin(\alpha R_j) \right.$$
$$\left. + \alpha x_j \sin(\alpha z_j) + \alpha \frac{y z_j}{R_j}\cos(\alpha R_j) - \alpha y \cos(\alpha z_j) \right], \quad (1)$$

$$B_{y,j} = \frac{1}{r_j^2}\left[y \frac{r_j^2}{R_j^3}\cos(\alpha R_j) - \alpha \frac{y z_j^2}{R_j^2}\sin(\alpha R_j) \right.$$
$$\left. + \alpha y \sin(\alpha z_j) - \alpha \frac{x_j z_j}{R_j}\cos(\alpha R_j) + \alpha x_j \cos(\alpha z_j) \right], \quad (2)$$

$$B_{z,j} = \frac{z_j}{R_j^3}[\cos(\alpha R_j) + \alpha R_j \sin(\alpha R_j)], \quad (3)$$

where $j = 1, 2$ designates the two poles and R_j is the distance from the position of the jth magnetic pole to the point at which $\boldsymbol{B}_j$ is calculated. Furthermore

$$R_j^2 = r_j^2 + z_j^2, \quad r_j^2 = x_j^2 + y^2, \quad (4)$$

$$x_j = x - x_{0,j}, \quad z_j = z - z_0. \quad (5)$$

The resultant magnetic field from the two opposite sign poles is then

$$B_x = A(B_{x,1} - B_{x,2}), \quad (6)$$

$$B_y = A(B_{y,1} - B_{y,2}), \quad (7)$$

$$B_z = A(B_{z,1} - B_{z,2}), \quad (8)$$

where $A = 1$ kG is the magnetic field intensity. We use different values for the α parameter. The coronal loop is added by tracing a single magnetic field line, and then using it as a central axis to construct a tube, which is filled with a higher-density plasma than the background value. The origin of this single field line, which varies depending on α, is chosen in order to maximize the sigmoidity of the resulting loop while keeping it in the simulation domain. The plasma density is gravitationally stratified in both the loop and the background. Note that the background plasma is hotter; therefore, the density scale height is higher than inside the loop. Thus, the ratio of densities inside and outside the loop is decreasing with height.

Note that the constructed cylindrical tube or loop is not tracing exactly a true flux tube, but it approximates one. In fact, starting from a circular cross section at one loop footpoint, the cross section of the flux tube gradually transitions to an elliptical shape toward the apex. In the case of nonzero α, the transition to an elliptical cross section is asymmetric, and results in an elliptical footpoint at the other end. This effect, which is more pronounced for higher values of α, is neglected in the present analysis. Moreover, the flux tube expands with height, which is easily accounted for in the zero-α setup, but it leads to nontrivial expansion for nonzero-α setups, therefore it is also neglected. The implications of this caveat on our results are discussed in Section 4.

Additionally, the weight of the higher-density loop is not counteracted by the force-free magnetic field initially, but the loop starts to fall by a small amount as we start the simulation. This leads to vertically polarized kink oscillations that coexist with the oscillations caused by impulsive horizontal driving at $t = 0$. The impulse is a velocity perturbation varying sinusoidally along the loop. The direction of the perturbation is defined by the horizontal perpendicular line to the loop axis in the apex, therefore it is not changing along the loop length. Using this driver, we aim to excite the fundamental standing kink mode of the loop. However, note that the initial perturbation probably does not coincide with the eigenfunction of the fundamental kink, which is not known. For example, in the case of a straight twisted flux tube, it is known that the plane of polarization for the fundamental kink eigenfunction is rotated along the tube (Ruderman & Terradas 2015). Therefore, while principally exciting the fundamental kink mode, other modes are also excited to a small degree, including leaky

Table 1
The Values of Principal Physical Parameters Used in the Simulations

Parameter	Value
Box size ($L \times 1 \times h$)	$100 \times 80 \times 70$ Mm
Pole depth and distance	$z_0 = 30$ Mm; $d = 30$ Mm
Traced field line origin	
(for increasing α) ($x, y, z = 0$)	(35,0); (38, −5); (38, −10); (40, −20) Mm
Values for the α-parameter	0,0.05,0.1,0.2
Loop radius at footpoint (R)	2.0 Mm
Loop footpoint density (ρ_{fi})	3.5×10^{-12} kg m^{-3}
Density ratio at footpoint (ρ_{fi}/ρ_{fe})	3
Loop temperature	1.0 MK
Background plasma temperature	3.0 MK
Average plasma β	0.018

waves. However, in this study, we only investigate the properties of the fundamental standing kink mode.

At the bottom boundary, we set reflective conditions for all three components of the velocity in order to mimic the line-tied conditions of a coronal loop anchored in the dense chromosphere and photosphere. The density and pressure are extrapolated to satisfy the hydrostatic equilibrium in the top and bottom boundaries. All other variables obey a zero-divergence, "continuous" condition. At the lateral boundaries all variables satisfy the "continuous" condition, thus leaving any leaky waves out of the simulation domain. The detailed values of the principal physical parameters are given in Table 1.

3. Numerical Method

The ideal MHD equations are solved in a 3D rectangular domain using MPI-AMRVAC 2.0 (Xia et al. 2018), with a finite-volume approach. We applied a splitting strategy for the magnetic field, where the time-independent magnetic field originating from the two "poles" is considered a force-free background field. Thus we only solve for the (nonlinear) perturbed magnetic field components. For this, we used the newly implemented HLLD solver adapted for magnetic field decomposition described in Guo et al. (2016). We use the available second-order "cada" slope limiter (Cada & Torrilhon 2009). The base resolution is $48 \times 32 \times 32$. We use four levels of refinement, with the refinement criteria being the density in Löhner's error estimator. A refinement study was not completed, however, based on our previous studies of kink oscillations (e.g., Magyar & Van Doorsselaere 2016); the period is not affected significantly by resolution. Resolution mostly affects the damping rates, which are not the focus of the present study. The solenoidal condition on the perturbed magnetic field is maintained by combining the implemented parabolic cleaner of Linde and Powell's divergence wave.[1]

4. Results and Discussion

Analysis of the oscillation properties is based on synthetic 171 Å intensity and Doppler shift images with the lines of sight corresponding to the coordinate axes (see Figure 2). Saving synthetic spectroscopic and imaging information about simulations is a built-in feature of MPI-AMRVAC. The magnetic field and density measurements are carried out along the single magnetic field line, which is used to construct the denser loop.

---

[1] See http://amrvac.org/md_doc_par.html for more information.

In order to infer magnetic field estimates seismologically, we need to calculate the theoretical kink speed. For a straight cylinder, this is defined as (Edwin & Roberts 1983)

$$c_k = \sqrt{\frac{\rho_i V_{A,i}^2 + \rho_e V_{A,e}^2}{\rho_i + \rho_e}}, \quad (9)$$

where V_A is the Alfvén speed, and the subscripts denote values inside and outside of the coronal loop. Then the period of the fundamental kink mode is given by

$$P = \frac{2L_{loop}}{c_k}, \quad (10)$$

where L_{loop} is the loop length, and the factor two signifies that the wavelength of the fundamental mode is double the loop length. However, a straightforward application of the above formula is not possible, as the kink speed is varying along the loop. Instead, we calculate the period using the WKB approximation:

$$P = 2 \int_{s_a}^{s_b} \frac{ds}{c_k(s)}, \quad (11)$$

where $s_{a,b}$ denote the two footpoints, and s is the coordinate along the loop axis. The measured and theoretically calculated periods are given in Table 2. The measured oscillation periods vary significantly for different α values. This variation is mostly explained by the maximal height of the loops, which is changing with α and the choice of the footpoint. The dipolar magnetic field is rapidly decreasing with height, thus lower-lying loops have a more intense magnetic field. As we can see, in the case of zero α, the match between the measured period and calculated period is exact. This demonstrates the robustness of Equation (11), even when applied to loops that do not satisfy the assumptions used in its calculation. For $\alpha = 0$, loop curvature, loop expansion, and gravitational stratification are the main additional factors. While the loop curvature does not appear to have a significant effect (van Doorsselaere et al. 2009), the other two factors are known to have a strong effect on the oscillation period. This is understandable, as both factors impact the Alfvén speed along the loop. For example, an expansion ratio of two (ratio of the tube radii at the apex and footpoints), as for $\alpha = 0$, would result in an increase of the fundamental mode period by more than a factor of two (Ruderman et al. 2008; Verth & Erdélyi 2008). This effect manifests in the decrease of the magnetic field toward the apex, and as such it is accounted for in Equation (11). In a similar manner, the effect of density stratification (Andries et al. 2005a, 2005b; Arregui et al. 2005) is thus also accounted for.

For the simulations with nonzero α, we see a general overestimation of the theoretical period which increases with α. As mentioned, for nonzero α we neglect the expansion and ellipticity of the flux tube. This implies that the filling factor (i.e., ratio of the higher-density loop cross section to the flux tube cross section) is decreasing with height, resulting in a lower average density inside the flux tube. Therefore, an overestimation of the period could be explained by the underestimation of the measured Alfvén speed, as the higher-density plasma is assumed to fill the whole flux tube in its calculation. However, this explanation is in contradiction with the observation that the period overestimation and the filling factor both grow with the value of α. While for $\alpha = 0.05$ the
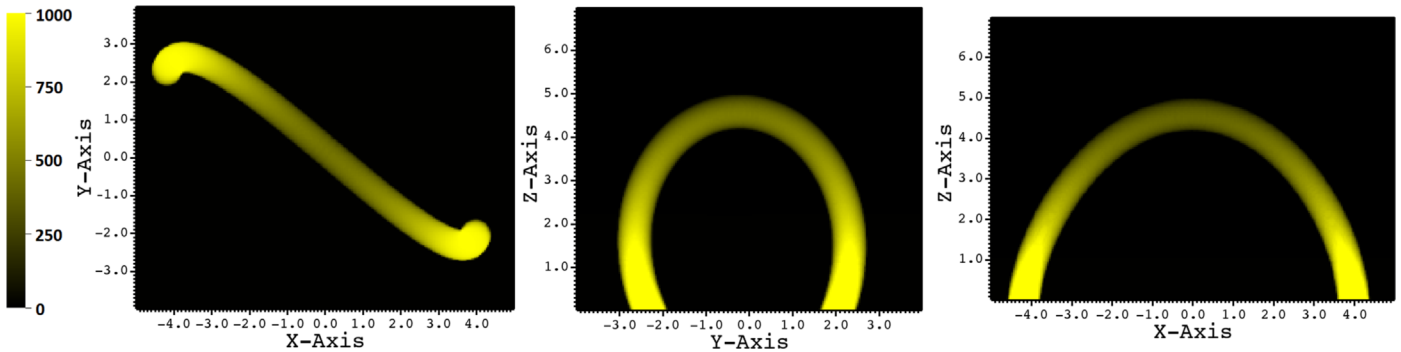
Figure 2. Synthetic AIA 171 Å images of the coronal loop for $\alpha = 0.2$, from three different viewpoints corresponding to the three coordinate axes. Values are in user units.

Table 2
The Measured Period, the Length of the Centrally Traced Loop Magnetic Field Line, and the Theoretical Oscillation Period Calculated from Equation (11)

α	Loop Length (Mm)	Period (s)	Theor. Period (s)
0	126.7	202.5	202.5
0.05	148.3	289.3	305.4
0.1	150.8	251	264.7
0.2	148.9	120.3	145.4

filling factor at the apex is 0.35, for $\alpha = 0.2$ the cross section of the flux tube, albeit highly elliptical and with a longer semimajor axis than the loop radius, has a smaller area than the higher-density loop. The cross-sectional ellipticity of the flux tube could also explain the overestimation of the period (Ruderman 2003; Erdélyi & Morton 2009). Ellipticity can lead to deviations in the fundamental kink period, proportional to its value, of up to 15% when compared to a circular cross-section model. However, in our model the ellipticity is varying along the flux tube, making a direct comparison to previous theoretical results difficult. On the other hand, while even for $\alpha = 0$ the flux tube is slightly elliptic at the apex, ellipticity in our model grows with the value of α, and therefore can be party considered as a direct result of the sigmoidity of the magnetic field. In this sense, in the present model we attribute the overestimation to the effect of sigmoidity of the magnetic field on the fundamental kink oscillation.

In the following, the implications for coronal seismology will be presented. The magnetic field intensity was determined using the measured oscillation period, loop length, and estimations of the density (Nakariakov & Ofman 2001):

$$B = \sqrt{\mu_0} \frac{\sqrt{2} L_{\text{loop}}}{P} \sqrt{\rho_i \left(1 + \frac{\rho_e}{\rho_i}\right)}, \qquad (12)$$

where μ_0 is the magnetic permeability. The results are shown in Figure 3. For the estimation of the range of the absolute value of the magnetic field using Equation (12) we have considered a range of an order of magnitude for the precision to which the average internal density can be determined. In the current model, the difference between the internal footpoint density and external apex density is less than an order of magnitude. We calculate this range by multiplying the measured average internal density with $10^{\pm 1/2}$. For the density ratio (ρ_i/ρ_e) we choose the range [1.5, 10]. In the simulation, the average density ratio is close to 2, varying along the loop and with the
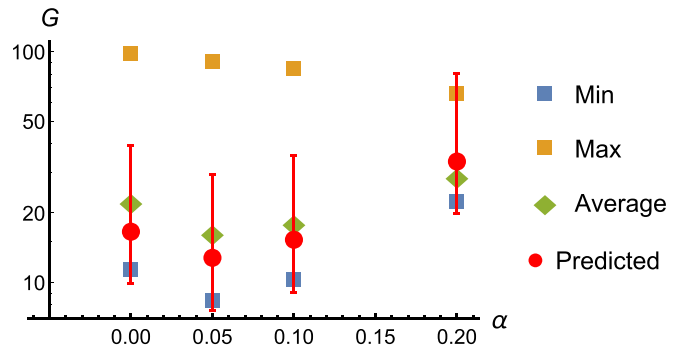

Figure 3. Plot showing the actual minimum, near the apex (blue square); maximum, near the footpoints (yellow square); average (green diamond); and seismologically estimated (red circle) magnitude of the magnetic field inside the oscillating loop, for different values of the α parameter. The seismologically estimated value uses the average value of internal density and density ratio. Values shown are for the single traced field line used to construct the loop. The average is taken over the full loop length. The error bar extends to the highest/lowest estimate resulting from the range of values considered for internal density and the density ratio (details in the text). Note that the ordinate axis is logarithmic.

value of α. Here we assume that the measurements of the length of the loop and of the period are exact.

For $\alpha = 0$, despite the similar measured and theoretically calculated periods, the seismologically predicted magnetic field value is lower than the average value. This discrepancy likely comes from the energy density distribution of the fundamental kink mode along the loop (Arregui et al. 2005), resulting in a weighting function of the form $\sin^2(\pi s/L_{\text{loop}})$, which lowers the effective average magnetic field along the loop. In other words, as the displacement amplitude of the fundamental mode has a maximum near the apex, the mode period is more sensitive to the magnetic field near the apex rather than near the footpoints. For increasing values of α, the predicted magnetic field shows an increasing trend relative to the average value, even surpassing it for $\alpha = 0.2$. This observation might give rise to the possibility of seismologically determining the sigmoidity of a coronal loop, if some other method to determine the average magnetic field is available, e.g., force-free extrapolations (Wiegelmann & Sakurai 2012). Additionally, a relatively accurate determination of the average density inside the loop and of the density ratio would be required. In this sense, the free magnetic energy in a coronal loop could be estimated seismologically. The resulting range for seismological estimation of the magnetic field, centered at a value that uses average values of the densities, lies almost entirely within the limits of

the measured magnetic field inside the loop. As explained previously, the estimated magnetic field range is shifted toward the minimum value, except for $\alpha = 0.2$, for which case it spans the entire range of magnetic field values measured in the loop.

5. Conclusion

We investigated the effects of coronal loop sigmoidity on the oscillation properties of the fundamental kink mode, and subsequently the impact on coronal seismology. We found that without sigmoidity, the calculated period using WKB theory agrees well with the period found in the simulation. However, increasing the value of α results in theoretical periods increasingly deviating from the measured period. We propose that this dependence could be exploited seismologically in order to measure the nonpotentiality, i.e., the free energy in coronal loops. However, for this method to work, the determination of the average magnetic field along the loop is needed, as well as an accurate measurement of the density along the loop. The average magnetic field could be approximated by, e.g., force-free source surface extrapolation using magnetograms (e.g., Wiegelmann & Sakurai 2012), while the density can be measured using, e.g., the emission line ratio method (e.g., Landi & Landini 1997). The external/internal density ratio is only weakly impacting the results. On the other hand, we demonstrated the robustness of the seismological method, even when applied to nonplanar or sigmoid coronal loops. For all values of sigmoidity considered, the estimation of the magnetic field is within the extremal magnetic field values measured in the loop, despite considering an order of magnitude accuracy for the average density determination.

ORCID iDs

N. Magyar ⓘ https://orcid.org/0000-0001-5731-8173
V. M. Nakariakov ⓘ https://orcid.org/0000-0001-6423-8286

References

Andries, J., Arregui, I., & Goossens, M. 2005a, ApJL, 624, L57
Andries, J., Goossens, M., Hollweg, J. V., Arregui, I., & Van Doorsselaere, T. 2005b, A&A, 430, 1109
Arregui, I., Van Doorsselaere, T., Andries, J., Goossens, M., & Kimpe, D. 2005, A&A, 441, 361
Aschwanden, M. J. 2019, ApJ, 874, 131
Aschwanden, M. J., Fletcher, L., Schrijver, C. J., & Alexander, D. 1999, ApJ, 520, 880
Aschwanden, M. J., Wuelser, J.-P., Nitta, N. V., et al. 2012, ApJ, 756, 124
Aschwanden, M. J., Wülser, J.-P., Nitta, N. V., & Lemen, J. R. 2008, ApJ, 679, 827
Cada, M., & Torrilhon, M. 2009, JCoPh, 228, 4118
Chiu, Y. T., & Hilton, H. H. 1977, ApJ, 212, 873
Cuperman, S., Ofman, L., & Semel, M. 1989, A&A, 216, 265
De Moortel, I. 2005, RSPTA, 363, 2743
De Moortel, I., & Nakariakov, V. M. 2012, RSPTA, 370, 3193
Dymova, M. V., & Ruderman, M. S. 2005, SoPh, 229, 79
Edwin, P. M., & Roberts, B. 1983, SoPh, 88, 179
Erdélyi, R., & Morton, R. J. 2009, A&A, 494, 295
Guo, X., Florinski, V., & Wang, C. 2016, JCoPh, 327, 543
Koskinen, H. E. J., Baker, D. N., Balogh, A., et al. 2017, SSRv, 212, 1137
Landi, E., & Landini, M. 1997, A&A, 327, 1230
Lanzerotti, L. J. 2017, SSRv, 212, 1253
Magyar, N., & Van Doorsselaere, T. 2016, A&A, 595, A81
McKenzie, D. E., & Canfield, R. C. 2008, A&A, 481, L65
McLaughlin, J. A., & Ofman, L. 2008, ApJ, 682, 1338
Miyagoshi, T., & Yokoyama, T. 2004, ApJ, 614, 1042
Nakariakov, V. M., & Ofman, L. 2001, A&A, 372, L53
Nakariakov, V. M., Ofman, L., Deluca, E. E., Roberts, B., & Davila, J. M. 1999, Sci, 285, 862
Nisticò, G., Polito, V., Nakariakov, V. M., & Del Zanna, G. 2017, A&A, 600, A37
Parnell, C. E., & De Moortel, I. 2012, RSPTA, 370, 3217
Pascoe, D. J., & De Moortel, I. 2014, ApJ, 784, 101
Reale, F. 2014, LRSP, 11, 4
Roberts, B., Edwin, P. M., & Benz, A. O. 1984, ApJ, 279, 857
Ruderman, M. S. 2003, A&A, 409, 287
Ruderman, M. S. 2007, SoPh, 246, 119
Ruderman, M. S., & Scott, A. 2011, A&A, 529, A33
Ruderman, M. S., & Terradas, J. 2015, A&A, 580, A57
Ruderman, M. S., Verth, G., & Erdélyi, R. 2008, ApJ, 686, 694
Schrijver, C. J., Aschwanden, M. J., & Title, A. M. 2002, SoPh, 206, 69
Scott, A., & Ruderman, M. S. 2012, SoPh, 278, 177
Singh, A. K., Siingh, D., & Singh, R. P. 2010, SGeo, 31, 581
Selwa, M., & Ofman, L. 2010, ApJ, 714, 170
Selwa, M., Ofman, L., & Solanki, S. K. 2011a, ApJ, 726, 42
Selwa, M., Solanki, S. K., & Ofman, L. 2011b, ApJ, 728, 87
Stepanov, A. V., Zaitsev, V. V., & Nakariakov, V. M. 2012, Coronal Seismology: Waves and Oscillations in Stellar Coronae Flare Plasma (Weinheim: Wiley-VCH Verlag GmbH & Co. KGaA)
Syntelis, P., Gontikakis, C., Georgoulis, M. K., Alissand rakis, C. E., & Tsinganos, K. 2012, SoPh, 280, 475
Terradas, J., & Goossens, M. 2012, A&A, 548, A112
Terradas, J., Oliver, R., & Ballester, J. L. 2006, ApJL, 650, L91
Uchida, Y. 1970, PASJ, 22, 341
Van Doorsselaere, T., Debosscher, A., Andries, J., & Poedts, S. 2004, A&A, 424, 1065
van Doorsselaere, T., Verwichte, E., & Terradas, J. 2009, SSRv, 149, 299
Verth, G., & Erdélyi, R. 2008, A&A, 486, 1015
Wiegelmann, T., & Sakurai, T. 2012, LRSP, 9, 5
Xia, C., Teunissen, J., El Mellah, I., Chané, E., & Keppens, R. 2018, ApJS, 234, 30
Zaitsev, V. V., & Stepanov, A. V. 1975, IGAFS, 37, 3
Zhou, G. P., Zhang, J., & Wang, J. X. 2016, ApJL, 823, L19